Tunable compact on-chip superconducting switch

Julia Zotova,[1,2,3,*] Alexander Semenov,[2,4] Rui Wang,[5,3] Yu Zhou,[3] Oleg Astafiev,[1,2] and Jaw-Shen Tsai[5,3,†]

[1] *Skolkovo Institute of Science and Technology, Moscow, 121205, Russia*
[2] *Moscow Institute of Physics and Technology, Institutskiy Pereulok 9, Dolgoprudny, 141701, Russia*
[3] *RIKEN Center for Quantum Computing, Wako, Saitama, 351-0198, Japan*
[4] *Moscow State Pedagogical University, Malaya Pirogovskaya Street 1/1, Moscow, 119435, Russia*
[5] *Research Institute for Science and Technology, Tokyo University of Science, 1-3 Kagurazaka, Shinjuku-ku, Tokyo, 162-8601, Japan*

(Received 28 September 2023; accepted 24 January 2024; published 29 February 2024)

We develop a compact four-port superconducting switch with tunable operating frequency in the range from 4.8 to 7.3 GHz. Isolation between channels exceeds 20 dB over a bandwidth of several hundred megahertz, exceeding 40 dB at some frequencies. The footprint of the device is $80 \times 420\ \mu m^2$. The tunability requires only a global flux bias without either permanent magnets or microelectromechanical structures. As the switch is superconducting, the heat dissipation during operation is negligible. The device can operate at up to -80 dBm, which corresponds to 2.5×10^6 photons per microsecond at a frequency of 6 GHz. The device shows the possibility to be operated as a beam splitter with tunable splitting ratio.

DOI: 10.1103/PhysRevApplied.21.024059

I. INTRODUCTION

Recently, superconducting quantum processors have demonstrated rapid progress, becoming more and more complex [1,2]. To solve computational problems, it is necessary to develop superconducting quantum processors with a large number of qubits [3–6], which results in large sizes of the processors. There are several approaches to increase the on-chip density of elements. Possible approaches with a fixed on-chip configuration include a flip chip [7], through-silicon-vias multilayer chip technology [8], and as a quasi-2D "origamilike" structure [9]. A different approach is a flexible circuit routing system, using "switch on-off" logic. On-demand routing allows one to calibrate a measurement setup [10] with fewer input-output channels, allows one to study on-chip transport as an alternative to split gates [11], and allows one to construct more-complex integrated quantum systems.

Commercially available mechanical pulse-latched switches based on semiconductors dissipate too much heat [10] to be compatible with millikelvin temperatures. For the same reason, temperature-activated switches [12] cannot be used in low-temperature experiments. Current-controlled positive-intrinsic-negative diode switches, and field-effect transistor diode switches with normally high insertion loss are also unsuitable for low-temperature experiments at powers of the single-photon level. In contrast, rf microelectromechanical switches [13,14] have low insertion loss, high isolation, and near-zero power consumption, as well as small sizes. However, because of the movement of the mechanical parts, this type of switch has a relatively slow switching time (2–40 μs), requires sophisticated fabrication techniques, and is very sensitive to humidity and organic contamination [15].

Fast switches based on nanowires in superconducting and normal states have been demonstrated [16]. They are also compact and broadband, but have high internal losses or parasitic reflections greater than 5 dB, which may not be sufficient for high-fidelity experiments. Also, cryotron switches [17], actuated by external current, exhibit fast switching (less than 200 ns) with high isolation (approximately 10^{-3}). However, such devices dissipate Joule heating (40 fW per switching) due to small parasitic resistances in the control line, making them difficult to use for multiqubit systems. Lower loss and higher isolation performance have been achieved with circuits using Josephson junctions and superconducting quantum interference devices (SQUIDs) as tunable inductance elements [18]. Some versions of switches based on Josephson junctions can also invert signals [19]. A scheme for multiplexed readout using this type of switch has been proposed and tested [19].

All the switches discussed are single-pole, single-throw switches. As a result, the use of these types of switch for on-chip routing may be limited, since only one channel is

*yuliya.zotova@phystech.edu
†tsai@riken.jp

involved. Single-pole, double-throw switches offer greater flexibility in controlling the propagation of the electromagnetic field. Proposals for such devices based on lumped elements have been demonstrated [18]. Also, a version using coplanar waveguides and a flux qubit as the coupling element [20] has been realized experimentally, however with relatively low isolation efficiency (62%) for its use in high-fidelity qubit operations. In addition, switching between signal paths using transmons has been demonstrated [21]. This single-photon router shows high isolation efficiency (approximately 92%) with fast switching (on the order of a few nanoseconds), but with small bandwidth (less than 50 MHz), which limits its wide use for multiqubit scaling. Even more flexibility in electromagnetic field steering is provided by two-input, two-output switches. The state-of-the-art implementation [22] gives high isolation and fast switching but it has a narrow bandwidth of up to approximately 150 MHz. That realization requires many on-chip components, including pairs of fixed-frequency hybrid beam splitters, frequency-tunable resonators with chains of SQUIDs and two dc lines to control the switching state. As a result, this device has a large size of 5×4 mm^2, limiting its wide use in on-chip multiqubit processors. In addition, all of the above-mentioned switches have a fixed operating frequency.

An alternative approach to signal routing is based on two coupled transmission lines. Fixed coupling has been used for a directional coupler [23] and microstrip-based networks [24]. In microwave photonics, only tunable coupling between resonators, not transmission lines, has been realized experimentally [25], showing the narrow bandwidth (approximately 50 MHz) with low frequency tunability (less than 1 GHz). However, in optical photonics, a switch based on tunable coupling between two suspended waveguides has been demonstrated [26]. The coupling is controlled by changing the physical distance between the lines by means of external voltage and cannot be varied over a wide range. This leads to a significant total length of the coupling section, which reaches 20 times that of the operating wavelength of $\lambda \sim 930$ nm. For microwave photonics with an operating frequency of 6 GHz on a silicon chip with $\varepsilon_{\mathrm{Si}} \sim 12$, this implies a structure length of 20×2 cm $= 40$ cm with the same coupling strength, making direct realization of such an approach in the microwave range impractical.

As one can see, there is a trade-off between sufficiently strong coupling, a reasonable structure size, and coupling tunability. At the same time, in microwave photonics, there have been no experimental realizations of a broadband on-chip two-input, two-output switch with frequency tunability suitable for signal routing. Moreover, we would like to make our device compact, i.e., smaller than the wavelength in coplanar waveguides at gigahertz frequencies ($\lambda_{\mathrm{CPW}} =$ 10–40 mm). We show that it is possible to solve all these problems at once by reducing the wavelength of the signal passing through the switch ($\lambda_{\mathrm{switch}} = 0.1$–$0.4$ mm). This is achieved by our choosing proper inductor and capacitor elements forming the lumped-element transmission lines of the switch.

The device has no moving parts, requires no pumping, and does not use standing waves, eliminating the size limitation of the structure. The device achieves high isolation of more than 40 dB; for a 20-dB threshold, the broadband range is several hundred megahertz. The insertion loss is less than a few decibels. The impedance change due to full-range tuning is within 0.2 Ω. The maximum operating power on the chip is −80 dBm, corresponding to 2.5×10^6 photons per microsecond at a frequency of 6 GHz, the highest maximum operating power to our knowledge for Josephson junction–based devices. Also, the device demonstrates tunability over a frequency range from 4.8 to 7.3 GHz with the above-mentioned isolation quality. The footprint of the device is 80×420 μm^2, and it requires only a single dc coil for control by external flux bias. The device dissipates a negligible amount of heat during operation, and does not increase the temperature of the mixing chamber stage. The device is fabricated by UV lithography and requires only electron-beam equipment for Josephson junction and parallel-plate capacitor fabrication [27]. This switch could provide flexible routing of electromagnetic fields, facilitate multiplexing and calibration, and help to scale up multiqubit processors or miniaturize current ones.

II. MODEL

The switch consists of two transmission lines with controllable coupling strength between them, as shown in Fig. 1(a). On the superconducting platform, there are many ways to realize both the transmission lines and the tunable coupling between them by configurable inductance and capacitance, as shown in Fig. 1(b). The inductance could be geometrical inductance (a wire), kinetic inductance (realized as thin films), or a Josephson inductance (represented by a Josephson junction). The capacitors could be either interdigital capacitors (large) or parallel-plate capacitors (compact). Tunable coupling could be realized by use of variable capacitance [26] or inductance, represented by kinetic inductance or a chain of SQUIDs, which could be biased by the external magnetic flux or local flux bias.

Next we present a theoretical model describing the operation of the device. We denote the inductance of a single transmission line of each unit as L and its capacitance as C. The coupling is represented by the mutual inductance of the lines, provided by the SQUID chain, L_{coup} per unit. For the given operating angular frequency $\omega = 2\pi f$, we find a relationship between the above-mentioned parameters and the required total number of units N to achieve a desired splitting ratio. The defined parameters and numbered ports are illustrated in Fig. 1(d).

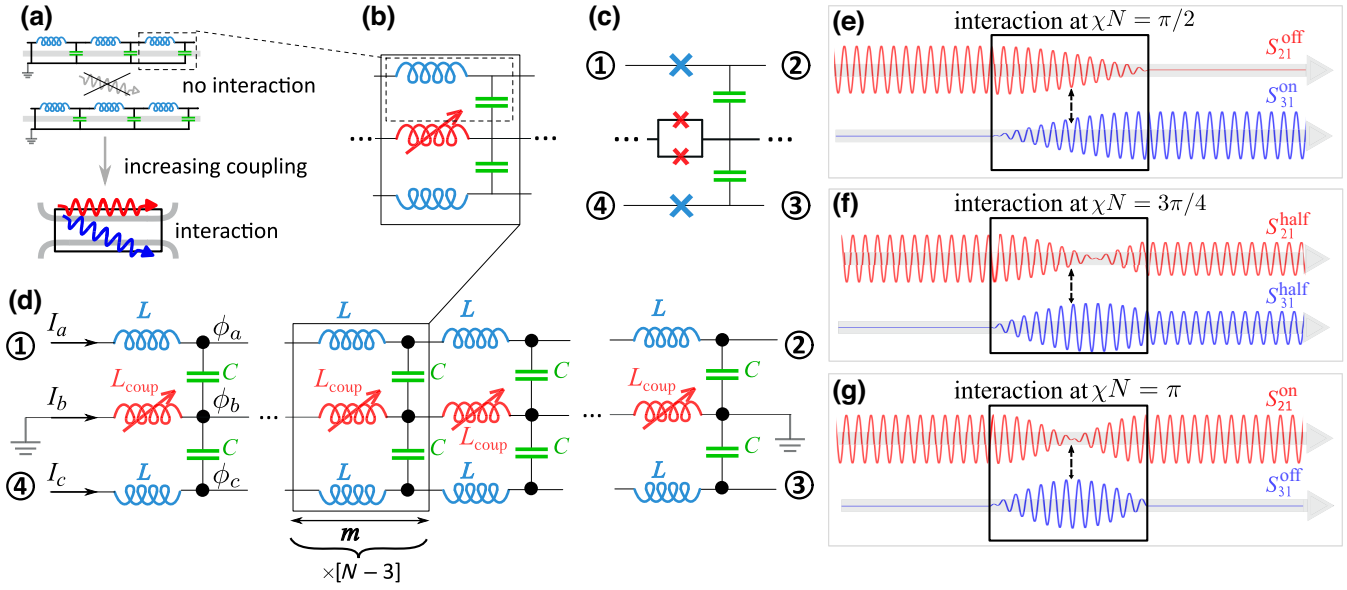

FIG. 1. Electric circuit and operating principle. (a) The four-port router with tunable coupling. (b) A lumped-element schematic realization of (a). (c) A realization of the scheme in (b) using compact components—Josephson junction inductors (blue), parallel-plate capacitors (green), and the tunable coupling as represented by SQUIDs (red). (d) The scheme used in the theoretical model. ϕ_a, ϕ_b, and ϕ_c are potentials at the particular node, and I_a, I_b, and I_c are current flows. (e)–(g) Cartoons of the three different regimes of switch states: S_{21}^{off}, $|S_{21}/S_{31}| = 1/2$, and S_{21}^{on} based on Eq. (6). In the interaction box, the signal is fully transmitted to the other channel at different lengths due to different coupling strengths χN.

The system of wave equations describing the circuit in the continuous limit is as follows:

$$\begin{aligned}\left(1+\tfrac{L_{\text{coup}}}{L}\right)\ddot{I}_a(n,t)+\tfrac{L_{\text{coup}}}{L}\ddot{I}_c(n,t)&=\tfrac{1}{CL}\tfrac{d^2I_a(n,t)}{dn^2},\\ \left(1+\tfrac{L_{\text{coup}}}{L}\right)\ddot{I}_c(n,t)+\tfrac{L_{\text{coup}}}{L}\ddot{I}_a(n,t)&=\tfrac{1}{CL}\tfrac{d^2I_c(n,t)}{dn^2}.\end{aligned} \tag{1}$$

With use of the Fourier transform of the current

$$I_{a,c}(k,\omega)=\int_{-\infty}^{+\infty}e^{j(kn-\omega t)}I_{a,c}(n,t)dndt, \tag{2}$$

the wave equation (1) becomes

$$\begin{aligned}I_a(k,\omega)\left(\left(1+\tfrac{L_{\text{coup}}}{L}\right)\omega^2-\tfrac{k^2}{LC}\right)+I_c(k,\omega)\tfrac{L_{\text{coup}}}{L}\omega^2=0,\\ I_a(k,\omega)\left(\tfrac{L_{\text{coup}}}{L}\right)\omega^2+I_c(k,\omega)\left(\left(1+\tfrac{L_{\text{coup}}}{L}\right)\omega^2-\tfrac{k^2}{LC}\right)=0.\end{aligned} \tag{3}$$

Equation (3) gives us two modes with the following dispersion relations for wave vectors:

$$\begin{aligned}k_+&=\pm\omega\sqrt{1+2\frac{L_{\text{coup}}}{L}}\sqrt{LC},\\ k_-&=\pm\omega\sqrt{LC}.\end{aligned} \tag{4}$$

When only transmission line a is excited at the input, the solution to Eq. (1) is

$$\begin{aligned}\begin{pmatrix}I_a\\ I_c\end{pmatrix}(n,t)&\sim\begin{pmatrix}e^{j(k_-n-\omega t)}+e^{j(k_+n-\omega t))}+\text{c.c.}\\ -e^{j(k_-n-\omega t)}+e^{j(k_+n-\omega t))}+\text{c.c.}\end{pmatrix}\sim\\ &\sim\begin{pmatrix}\cos(Kn-\omega t)\cos(\chi n)\\ -\sin(Kn-\omega t)\sin(\chi n)\end{pmatrix},\end{aligned} \tag{5}$$

where $K=0.5(k_-+k_+)$ and $\chi=0.5(k_--k_+)$ show how the current oscillates: K is the high-frequency carrier signal and χ is the low-frequency envelope. The phase factors of the currents of outputs 2 and 3 are equal to $\cos(Kn-\omega t)$ and $-\sin(Kn-\omega t)$ [see Eq. (5)], so the phase difference between them is equal to $-\pi/2$ and does not depend on the magnetic field.

For powers in output ports S_{21} and S_{31}, after our averaging out over time the high-frequency component K, only the envelope χ for the oscillating current is left:

$$\begin{aligned}S_{12}&\sim\langle I_a^2(N)\rangle\sim\cos^2(\chi N),\\ S_{13}&\sim\langle I_c^2(N)\rangle\sim\sin^2(\chi N).\end{aligned} \tag{6}$$

The phase of the envelope signal determines how much of the signal passes to another channel. For the fully transmitted signal, see Fig. 1(e), $I_a=0\Rightarrow\cos(\chi N)=0$ and

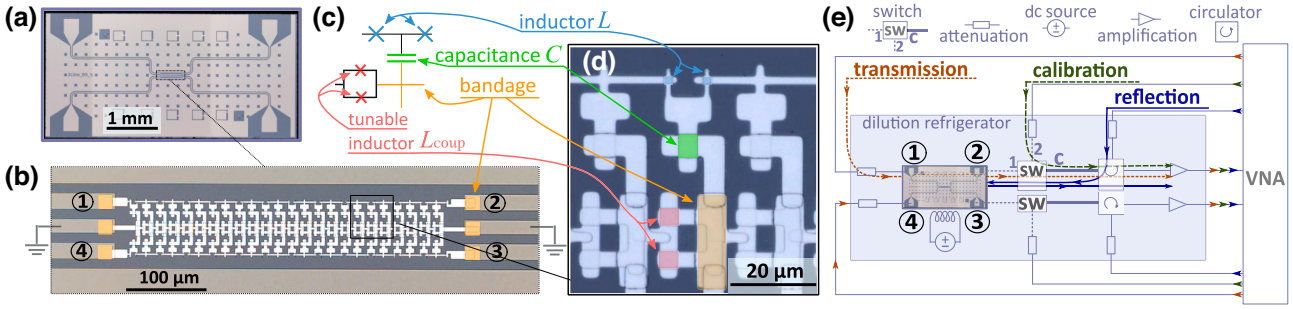

FIG. 2. The chip and the measurement scheme. (a) Micrograph of the chip, (b), (d) enlarged parts, and (c) the equivalent electric scheme. The Josephson junction inductors (blue) and the capacitors (green) of each transmission line unit are shown. The Josephson junction inductors, forming SQUIDs, are shown in red. Beige squares indicate bandages for robust galvanic contact. (e) Measurement setup with the dilution refrigerator. Different colors of arrows indicate the path for the different measurement routes: transmission along the structure (dashed dark-orange line), reflection (solid dark-blue line), and calibration channel (dashed dark-green line). Filters, isolators, and the distribution of microwave components across refrigerator stages are omitted. The state of the commercial switch (sw) is different for transmission-reflection ("1") and calibration ("2") measurement with common output ("c"). The setup is horizontally symmetrical along the chip. Microwave signals are generated and detected by vector network analyzer (VNA).

$I_c = I_{\max} \Rightarrow \sin(\chi N) = \pm 1$, so the coupling phase

$$\chi N = \frac{1}{2}\left(\sqrt{1 + 2\frac{L_{\text{coup}}}{L}} - 1\right)\sqrt{LC}\omega N = \frac{\pi}{2}. \quad (7)$$

For other cases, such as equal splitting [Fig. 1(f)] and return transmission to the first channel [Fig. 1(g)], $\chi N = 3\pi/4$ and $\chi N = \pi$, respectively. Note that only the phase of the envelope signal at the output is important for the switching state, regardless of the number of oscillations passing through the system on the coupling length. Since the device is horizontally symmetric and the coupling between the lines is described by a scalar parameter—the inductance—we expect the same behavior when we swap between inputs 1 and 4 and between outputs 2 and 3. If we apply signals to both inputs simultaneously, due to the linearity of the device, we expect the result to be equal to the sum of the corresponding complex amplitudes at the outputs; see Eq. (5).

The desired parameters of the device that fulfill the conditions Eq. (7) and impedance match $Z = \sqrt{L/C} = 50\ \Omega$ are chosen by our taking into account the fabrication considerations, which we discuss further later. The choice of a particular inductor realization may require further refinement of the equations. In this paper, we present only a compact realization of the scheme; see Fig. 1(c). To implement the inductors, we use Josephson junctions, which have an internal capacitor. The line inductance L^* and the coupling inductance L^*_{coup} including the effect of the Josephson junction capacitance are given by

$$\begin{aligned} 1/L^* &= 1/L - \omega^2 C_{\text{JJ}}, \\ 1/L^*_{\text{coup}} &= 1/L_{\text{coup}} - \omega^2 C_{\text{SQUID}}. \end{aligned} \quad (8)$$

The inductance of each Josephson junction in the lines can be described by $L \approx \Phi_0/(2\pi I_c)$ and the inductance of each SQUID can be described by $L_{\text{coup}} \approx \Phi_0/(4\pi I_c\sqrt{\cos(\pi\Phi/\Phi_0)})$, where Φ_0 is the magnetic flux quantum. These analytical expressions are valid as long as the currents flowing through the junctions are small compared with their critical values I_c. This leads to a limit in the working power, which we discuss in the next section.

III. DEVICE REALIZATION

In this section we present chip parameters and low-temperature measurement results. The chip and the equivalent electric scheme of the circuit are shown in Figs. 2(a)–2(d). Coplanar 50-Ω waveguides for signal routing and flux traps for stabilizing the magnetic field are formed on a silicon chip of 5×2.5 mm^2. They are made of sputtered 50-nm niobium film followed by reactive-ion etching in CF_4. The Josephson junctions (blue and red) and capacitors (green) [27] consist of an aluminum–aluminum oxide–aluminum trilayer in two separate lithography runs with thicknesses of 50–80 nm each. To provide a robust galvanic contact between several metallic layers, bandages (beige) are used. They are made of 100-nm-thick aluminum film with heavy argon milling before deposition to remove native oxidation layers of aluminum and niobium. All aluminum structures are deposited by electron-beam evaporation and oxidation in a Plassys MEB550S3 evaporator. Pattering is done by standard photolithography techniques and all aluminum structures are fabricated by lift-off. The area of the transmission line Josephson junctions is 1.8 μm^2, the area of the capacitor is 22 μm^2, the area of the SQUID is 26.4 μm^2, and their junction areas are each 12.6 μm^2. The entire structure, consisting of $N = 24$ units, has a size of 80×420 μm^2. To achieve a mirror-symmetric structure, we retain the total inductance of the

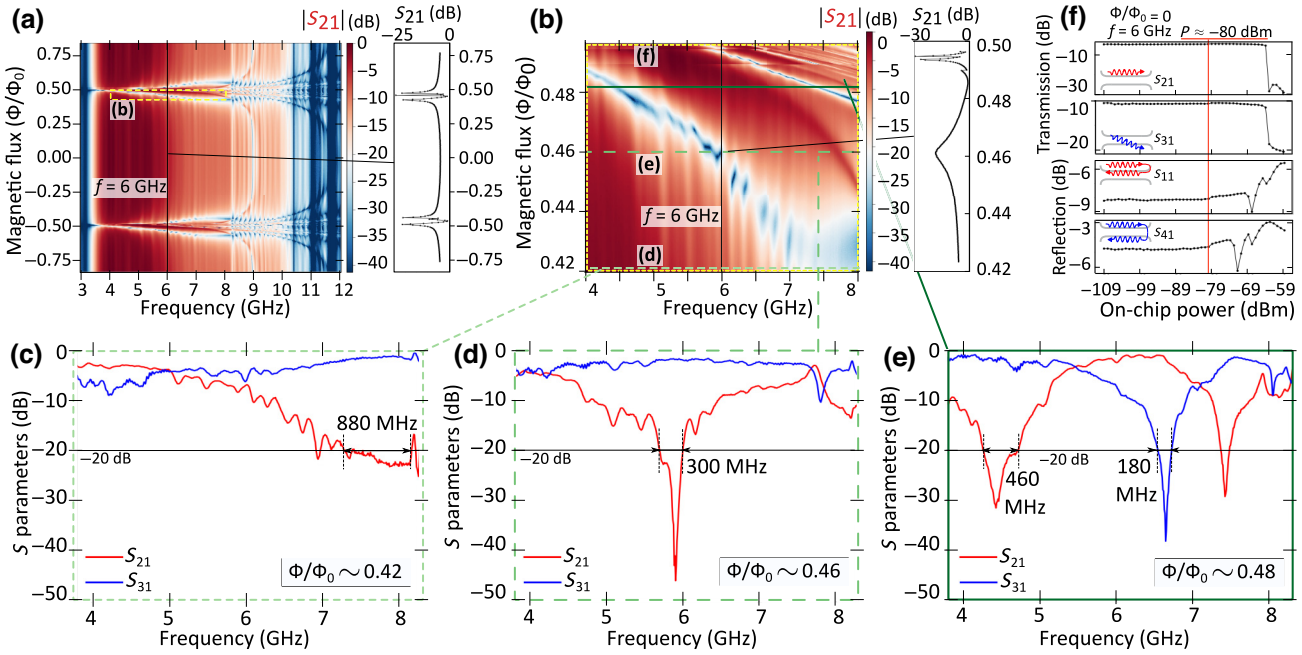

FIG. 3. Selection of working magnetic field and power. (a) Magnitude of complex transmission $|S_{21}|$ of the device as a function of frequency and magnetic flux with the cross section at 6 GHz with in a separate box (black). (b) Enlarged area of a fragment of the periodic pattern near $\Phi/\Phi_0 = 0.5$ with the cross section at 6 GHz in a separate box (black). (c)–(e) $|S_{21}|$ and $|S_{31}|$ as a function of frequency for different magnetic fields. The horizontal black line indicates the −20-dB isolation threshold. (f) Magnitude of raw complex transmission and reflection coefficients ($|S_{21}|$, $|S_{31}|$, $|S_{11}|$, and $|S_{41}|$) as a function of applied power at 6 GHz at $\Phi/\Phi_0 = 0$. The vertical red line is the threshold (−80 dBm on-chip power) for the linear response.

Josephson junction of the edged unit in the transmission line but divide it into two Josephson junctions at the left and right edges. We realize this by changing the junction area; also, we omit the edged SQUID as it is shunted. We also implement the switches using large components (a wire inductor with $S_L \sim 7600\ \mu m^2$ and an interdigitated capacitor with $S_C \sim 34\,000\ \mu m^2$). We find that for large components transmission is too inhomogeneous and has poor isolation. This is probably due to irregular ground potential over several millimeters, crosstalk, or the size of each unit being not too small in comparison with the operating wavelength. Because of the poor performance of a large-component device, we present only a compact realization and we emphasize the need for compact components, especially capacitors [27].

Using test Josephson junctions and bandages, placed on the same chip, we check their electric characteristics by measuring room-temperature resistance R_n'. Using the Ambegaokar-Baratoff relation $I_c = \Delta\pi/(2eR_n)$, where R_n is the normal state resistance and Δ is the superconducting gap, we estimate the inductance of each Josephson junction $L = \Phi_0/(2\pi I_c)$. We note that $R_n < R_n'$, but for estimation we use $R_n = R_n'$ and get $L = 0.28$ nH/unit.

For the resistance measurement, we consider the reference resistance of the bandage structure with its interface, $R \sim 42\ \Omega$. For capacitors, we estimate the capacitance C of each unit as $S \times c$ as the product of the fabricated area S, obtained with use of an optical microscope, and the capacitance per unit area c, which we obtained experimentally under similar conditions [27]. We find that the capacitance C per unit circuit is approximately 300 fF. According to our estimates, the stray capacitance is negligible compared with that value. Using parameters L, C, and the linear size of the unit $m = 34\ \mu$m, we estimate the characteristic impedance $Z = \sqrt{L/C} \sim 30\ \Omega$, the constant part of the phase velocity $v_{\rm ph}^{\rm const} = m\omega/k_- = m/\sqrt{LC} = 3.4 \times 10^6$ m/s, and the variable part of the phase velocity

$$v_{\rm ph}^{\rm var} = m\omega/k_+ = m/\left(\sqrt{1 + 2\frac{L_{\rm coup}}{L}}\sqrt{LC}\right), \qquad (9)$$

which we numerically estimate at the end of Sec. IV after fitting the measurement data. The slow phase velocity is the key feature of this transmission line, since it limits the spatial size of the device. In the case of a conventional transmission line, the device will be large as the phase velocity is faster, and is more than 5 mm long.

IV. MEASUREMENT RESULTS

The chip is mounted at the base stage of a dilution refrigerator at a temperature of 12 mK. The signal from a vector network analyzer is attenuated and filtered before entering

the chip and being amplified at the output. The raw magnitudes of the complex transmission coefficients $|S_{21}|$ and $|S_{31}|$ are obtained under continuous wave excitation, generated by the vector network analyzer, and then calibrated by the separate path in the cable setup; see the measurement scheme in Fig. 2(e). The measurement setup inside the dilution refrigerator consists of two nominally identical sets of an input line for the transmission measurement (dashed dark-orange line), an input line and a circulator for reflection measurement (solid dark-blue line), and a line for calibration (dashed dark-green line). These three paths are connected by a commercial switch, and one can select transmission, reflection, or calibration using the same source of microwave signals. Calibration takes into account the path from the commercial switch to the output; therefore, cables, connectors of the sample holder, and bonds between the chip and the commercial switch affect the calibrated results by about a few decibels. We present the results in the range from 4 to 8 GHz limited by our circulator bandwidth. When the fourth port is not used, it is terminated with a 50-Ω load.

First, we obtain the flux-dependent response of the S parameters [see Figs. 3(a) and 3(b) for $|S_{21}|$]. We measure $|S_{21}|$ and $|S_{31}|$ as a function of frequency and external magnetic flux applied by the coil. We observe a periodic pattern, which is expected from the periodic behavior of the Josephson energy and inductance of SQUIDs with changing magnetic flux. One period of the pattern of $|S_{21}|$ is shown in Fig. 3(a), with a vertical slice of the data at 6 GHz in black. The transmission changes a little from $\Phi/\Phi_0 = 0$ to almost 0.4, but changes radically when approaching half-flux quantum. An enlarged part of the $|S_{21}|$ spectrum for $\Phi/\Phi_0 = 0.42$–0.50 is shown in Fig. 3(b), with the section at 6 GHz in black. The resonance peaks shift towards lower frequencies as the inductance of the coupling SQUIDs increases with increasing magnetic flux, as shown in Figs. 3(b)–3(e). The area near $\Phi/\Phi_0 \sim 0.5$ has the sharpest transmission changes, where the inductance of each SQUID undergoes the largest changes and the maximum value is limited only by the asymmetry of the Josephson contacts. Figures 3(c)–3(e) show calibrated $|S_{21}|$ (red) and $|S_{31}|$ (blue) transmissions for different magnetic fluxes $\Phi/\Phi_0 = 0.42$ [Fig. 3(c), dashed green line], $\Phi/\Phi_0 = 0.46$ [Fig. 3(d), dashed green line], and $\Phi/\Phi_0 = 0.49$ [Fig. 3(e), solid green line]. The data show a broadband transmission of 0.2–1 GHz for the operating regime with at least 20 dB of isolation, exceeding 40 dB for some frequencies. Transmission is slightly below the unit level, likely due to impedance mismatch and an imperfect calibration procedure.

We also estimate the linear power operating range of our device; see Fig. 3(f). At $\Phi/\Phi_0 = 0$ and $f = 6$ GHz, we plot the longitudinal $|S_{21}|$ and transverse $|S_{31}|$ transmission coefficients and the longitudinal $|S_{11}|$ and transverse $|S_{41}|$ reflection coefficients as a function of the on-chip power, which is estimated with use of the calibration protocol mentioned above. We find that the device exhibits linear behavior up to approximately -80 dBm, which is indicated by the vertical red line. This power is equivalent to 10 pW, corresponding to 2.5×10^6 photons per microsecond at a frequency of 6 GHz, which is sufficient not only for qubit and single-photon experiments but also for high-power purposes, such as pumping and driving qubit systems. The sharp drop in the transmission coefficients $|S_{21}|$ and $|S_{31}|$ at around -65 dBm of applied power corresponds to exceeding the critical current through Josephson junctions in the transmission line, where the analytical expression for the inductance of the Josephson junction is not valid and active losses occur. In general, the upper limit of the operating power can be increased if the number of units N is increased with successive increases in the critical current of each Josephson junction, keeping the total inductance of the SQUID chain the same. We assume that for other magnetic fields the device will still be in a linear regime below the threshold power, since the device linearity is determined by the linearity of the transmission line Josephson junctions. This is because their critical current is 10 times smaller than that of SQUIDs.

Next we discuss the switching quality. We plot $|S_{21}|$ and $|S_{31}|$ as a function of external normalized magnetic flux at different operating frequencies in the working range: 4.8, 5.5, 6.0, 6.5, 7.0 GHz in Fig. 4. The plots are vertical cutplots of Fig. 3(b) for calibrated S_{21} and S_{31}. As one can see, the curves in each panel in Fig. 4 continuously change from one panel to the next as the frequency changes, giving us an understanding of what the S parameters are like at other frequencies within the operating range. The isolation for $|S_{31}|$ and $|S_{21}|$ for each frequency exceeds 20 dB, which is indicated by the horizontal black line in each plot in Fig. 4. The possible operating points of the device are indicated by red and blue arrows, accordingly. At low magnetic flux, the transmission minimum is shallower compared with that at stronger fields, but is smoother and less sensitive to changes of the magnetic field, such as noise caused by flux jumps or instability of a current source. Depending on the requirements—higher isolation or insensitivity to magnetic noise—different magnetic flux points should be chosen. Also, at $\Phi/\Phi_0 = 0.49$–0.50 at high frequencies we observe jumps in transmissions that may be caused by inhomogeneities of critical currents in the SQUIDs, forming coupling between transmission lines. Also, the data demonstrate the device can operate as a beam splitter with splitting of equal ratio or an arbitrary ratio and low loss of less than 1 dB, although the bandwidth is narrow. We cannot precisely measure the absolute value of the phase difference between the outputs, but we observe a constant value as a function of the magnetic flux; see Fig. 4 (green). The value is different for different frequencies, so the data are shifted to the theoretical reference of -90° for clarity.

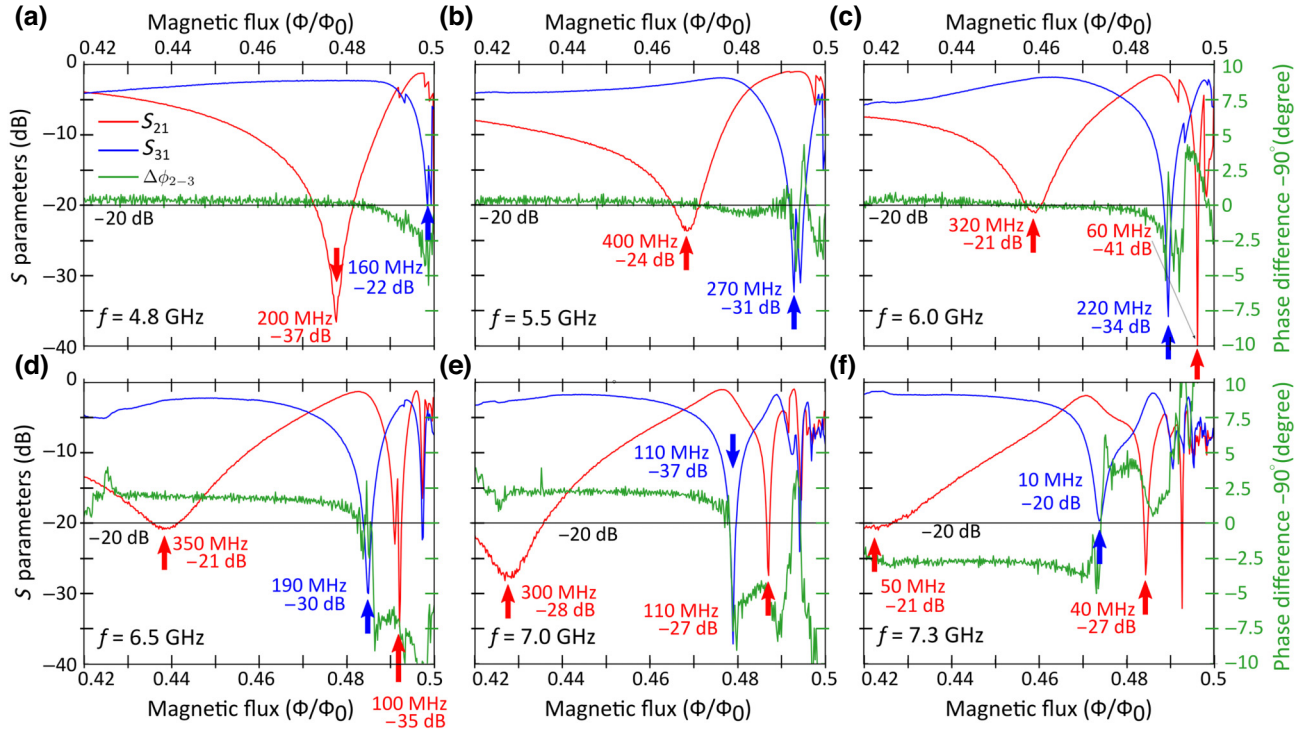

FIG. 4. Switching performance for different frequencies. Calibrated magnitude of complex transmission coefficients $|S_{21}|$ (red) and $|S_{31}|$ (blue) for each frequency with varying magnetic flux, generated by the global coil. The horizontal black line shows the −20-dB level, and the red and blue arrows indicate possible working points of switching to the desired state. The bandwidth and isolation are also shown at these points. The green line shows the phase difference between output ports 2 and 3.

The phase data shows a negligible spread of less than 10° in the working range of the magnetic flux.

Below we discuss the fitting model for S parameters and investigate the coupling phase between two transmission lines as a function of different magnetic fields. Using Eq. (6), we extract χ from the experimental data as a function of frequency for different magnetic fluxes, indicated by different intensity of green color and plot the coupling phase $\chi N/\pi$ in Fig. 5(a) as dots. We select the same frequency range as for the switching quality demonstration, i.e., 4.8–7.3 GHz. Next we fit the data using Eqs. (7) and (8) and extract the effective inductance L^*_{coup} of each unit; see Fig. 5(a), dashed lines. Using the extracted values of L^*_{coup}, we calculate the coupling phase of all other current values and use it for further numerical calculations. We plot the isolation ratio of the measured S parameters $S_{21} - S_{31}$ as a function of frequency and applied external magnetic flux; see Fig. 5(b). The isolation ratio of the S parameters is then calculated with use of Eqs. (6)–(8) and the fitting data from Fig. 5(a) as a function of frequency and magnetic flux; see Fig. 5(c). We see that the model describes the qualitative S parameters well, with a small inhomogeneous discrepancy, which could be explained by the nonideal identity of the coupling SQUIDs. The difference between the absolute numerical values of the calculated isolation ratio and the measured isolation ratio could be explained by nonzero parasitic reflections, possible dielectric losses, and rf crosstalk between the channels. In general, the plots in Figs. 5(b) and 5(c) show that each frequency in the working range from 4.8 to 7.3 GHz has the maximum and the minimum value of the isolation ratio, corresponding to the open and closed states for each output of the switch. In addition, increasing the magnetic field, and hence the coupling inductance, results in a decrease in the variable component of the phase velocity [Eq. (9)] $v_{\mathrm{ph}}^{\mathrm{var}}$ from 2.75×10^6 to 2.07×10^6 m/s and a decrease in the characteristic impedance Z by 0.5% according to $Z = 0.5(\sqrt{1 + 2L_{\mathrm{coup}}/L} + 1)\sqrt{L/C}$.

Finally, we discuss the characteristic time of switching between the channels and changing operating frequencies. The presented device is controlled by an external magnetic field, generated by a coil with a large coil inductance. In this case the switching time is limited by the characteristic rise time of the coil. To make the switching time shorter, high-frequency current bias lines should be implemented on-chip similar to the ones used to control energies of a superconducting qubit with SQUID loops. The pulses in the matched broadband line are limited by tens of picoseconds. In practice, the switching time in this case is limited by the speed of an arbitrary waveform generator. Devices based on a SQUID chain can change their characteristics in nanoseconds [28]. The minimal possible

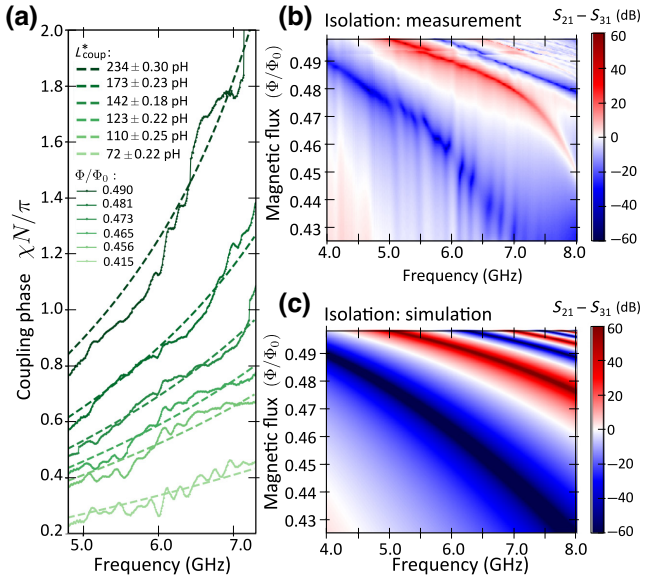

FIG. 5. Fitting of coupling phase and numerical calculations of the model. (a) Coupling phase between two transmission lines as a function of frequency for different magnetic fluxes. The dotted lines represent data extracted with use of Eq. (6) and the dashed lines are fits obtained with Eqs. (7) and (8). (b) Isolation ratio as a function of frequency for different magnetic fluxes of the calibrated S parameters, calculated as $S_{21} - S_{31}$. (c) Numerical calculation of the isolation ratio of the S parameters [Eqs. (6) and (7)] as a function of frequency for different magnetic fluxes.

switching time is limited by the transient processes in each SQUID in response to the magnetic field, which we estimate as the inverse Josephson-junction plasma frequency $\tau_{JJ} = 1/\omega_p = \sqrt{L^*_{coup} \times C_{SQUIDs}} \sim 12$ ps. The switching time also depends on a propagation time along the coupling length: $\tau_{1\text{-}2} = mN/v_{ph}^{const} \approx 124$ ps or $\tau_{1\text{-}3} = mN/v_{ph}^{var} \approx 101 - 76$ ps depending on the magnetic field, where the phase velocity is determined by Eq. (9). The total exact switching time $\tau = \tau_{JJ} + \tau_{1\text{-}2}$ (or $\tau = \tau_{JJ} + \tau_{1\text{-}3}$) depends on the magnetic field, and for simplicity, we can determine the switching time by the longest delay as $\tau = 136$ ps.

V. CONCLUSION

We describe the design, realization, and characterization of a switch, based on two transmission lines, coupled by a tunable inductor, implemented by a chain of SQUIDs. We experimentally demonstrate that the operating frequency is tunable over the range from 4.8 to 7.3 GHz with a bandwidth of a few hundred megahertz. For a given bandwidth, the isolation exceeds 20 dB and reaches 40 dB. The working power ranges up to −80 dBm on-chip, corresponding to 2.5×10^6 photons per microsecond (10 pW) at a frequency of 6 GHz. The device size is 80×420 μm^2, and it is controlled by external flux bias with local dc-line control capability. The impedance change due to tuning is within 0.2 Ω. The fabrication of the investigated device requires only well-established fabrication techniques, such as photolithography and electron-beam deposition and oxidation. The switching time is limited by the external magnetic control, such as the speed of the current change in a coil. Operating at the base temperature of a dilution refrigerator, the switch does not heat the circuit.

To improve the performance of the device, e.g., as to increase the working frequency range, and to avoid approaching $\Phi_0/2$ due to flux jumps, a reasonable strategy is to increase the number of units N, while keeping other parameters the same. Increasing L_{coup} itself by reducing the critical current I_c of the Josephson junctions forming the SQUIDs also leads to the same results, but at the same time it causes a decrease in the working power limit. Future work could aim at fast control using local bias, as this could reduce the switching time. The bias lines could be implemented by use of the air-bridge technology [29]. In this case operation will be possible with multiple devices on the same chip, opening a door to many microwave multiplexing applications and configurable network schemes. The device can be used to control and read out superconducting quantum systems with fewer cables. In addition, there is a possibility of operating the device in the quantum regime, by using a single-photon source [30]. The device shows the possibility to be operated as a mirror (or a beam splitter) with tunable splitting ratio, and future research could be dedicated to investigation of the efficiency of the splitting and applications in linear optics schemes.

ACKNOWLEDGMENTS

J.Z. is grateful to Hiroto Mukai, Ilya Besedin, and Gleb Fedorov for stimulating discussions. This work was funded by the RIKEN International Program Associate program, by the ImPACT program of the Council for Science, Technology and Innovation (Cabinet Office, Government of Japan), by the CREST program of the JST (Grant No. JPMJCR1676), and by the New Energy and Industrial Technology Development Organization, (Grant No. JPNP16007). J.Z. is grateful to the support of the Russian Science Foundation (Grant No. 21-72-30026; see Ref. [31], data analysis). A.S. is grateful to the support of the Russian Science Foundation (Grant No. 21-72-10117, theory).

[1] Morten Kjaergaard, Mollie E. Schwartz, Jochen Braumüller, Philip Krantz, Joel I.-J. Wang, Simon Gustavsson, and William D. Oliver, Superconducting qubits: Current state of play, Annu. Rev. Condens. Matter Phys. **11**, 369 (2020).

[2] Michel H. Devoret and Robert J. Schoelkopf, Superconducting circuits for quantum information: An outlook, Science **339**, 1169 (2013).

[3] Frank Arute, Kunal Arya, Ryan Babbush, Dave Bacon, Joseph C. Bardin, Rami Barends, Rupak Biswas, Sergio Boixo, Fernando G. S. L Brandao, David A. Buell, *et al.*,

Quantum supremacy using a programmable superconducting processor, Nature **574**, 505 (2019).

[4] Yulin Wu, Wan-Su Bao, Sirui Cao, Fusheng Chen, Ming-Cheng Chen, Xiawei Chen, Tung-Hsun Chung, Hui Deng, Yajie Du, Daojin Fan, *et al.*, Strong quantum computational advantage using a superconducting quantum processor, Phys. Rev. Lett. **127**, 180501 (2021).

[5] Wenhui Ren, Weikang Li, Shibo Xu, Ke Wang, Wenjie Jiang, Feitong Jin, Xuhao Zhu, Jiachen Chen, Zixuan Song, Pengfei Zhang, *et al.*, Experimental quantum adversarial learning with programmable superconducting qubits, Nat. Comput. Sci. **2**, 711 (2022).

[6] Ming Gong, Shiyu Wang, Chen Zha, Ming-Cheng Chen, He-Liang Huang, Yulin Wu, Qingling Zhu, Youwei Zhao, Shaowei Li, Shaojun Guo, *et al.*, Quantum walks on a programmable two-dimensional 62-qubit superconducting processor, Science **372**, 948 (2021).

[7] B. Foxen, J. Y. Mutus, E. Lucero, R. Graff, A. Megrant, Yu Chen, C. Quintana, B. Burkett, J. Kelly, E. Jeffrey, *et al.*, Qubit compatible superconducting interconnects, Quantum Sci. Technol. **3**, 014005 (2017).

[8] Donna-Ruth W. Yost, Mollie E. Schwartz, Justin Mallek, Danna Rosenberg, Corey Stull, Jonilyn L. Yoder, Greg Calusine, Matt Cook, Rabindra Das, Alexandra L. Day, *et al.*, Solid-state qubits integrated with superconducting through-silicon vias, npj Quantum Inf. **6**, 1 (2020).

[9] Hiroto Mukai, Keiichi Sakata, Simon J. Devitt, Rui Wang, Yu Zhou, Yukito Nakajima, and Jaw-Shen Tsai, Pseudo-2D superconducting quantum computing circuit for the surface code: Proposal and preliminary tests, New J. Phys. **22**, 043013 (2020).

[10] Leonardo Ranzani, Lafe Spietz, Zoya Popovic, and José Aumentado, Two-port microwave calibration at millikelvin temperatures, Rev. Sci. Instrum. **84**, 034704 (2013).

[11] H. Al-Taie, L. W. Smith, B. Xu, P. See, J. P. Griffiths, H. E. Beere, G. A. C. Jones, D. A. Ritchie, M. J. Kelly, and C. G. Smith, Cryogenic on-chip multiplexer for the study of quantum transport in 256 split-gate devices, Appl. Phys. Lett. **102**, 243102 (2013).

[12] Nabil El-Hinnawy, Pavel Borodulin, Brian P. Wagner, Matthew R. King, Evan B. Jones, Robert S. Howell, Michael J. Lee, and Robert M. Young, Low-loss latching microwave switch using thermally pulsed non-volatile chalcogenide phase change materials, Appl. Phys. Lett. **105**, 013501 (2014).

[13] Songbin Gong, Hui Shen, and N. Scott Barker, Study of broadband cryogenic DC-contact RF MEMS switches, IEEE Trans. Microw. Theory Tech. **57**, 3442 (2009).

[14] Sara S. Attar, Sormeh Setoodeh, Raafat R. Mansour, and Deepnarayan Gupta, Low-temperature superconducting DC-contact RF MEMS switch for cryogenic reconfigurable RF front-ends, IEEE Trans. Microw. Theory Tech. **62**, 1437 (2014).

[15] Gabriel M. Rebeiz and Jeremy B. Muldavin, RF MEMS switches and switch circuits, IEEE Microw. Mag. **2**, 59 (2001).

[16] Andrew Wagner, Leonardo Ranzani, Guilhem Ribeill, and T. A. Ohki, Demonstration of a superconducting nanowire microwave switch, Appl. Phys. Lett. **115**, 172602 (2019).

[17] Peter J. Lowell, John A. B. Mates, W. Bertrand Doriese, Gene C. Hilton, Kelsey M. Morgan, Daniel S. Swetz, Joel N. Ullom, and Daniel R. Schmidt, A thin-film cryotron suitable for use as an ultra-low-temperature switch, Appl. Phys. Lett. **109**, 142601 (2016).

[18] Ofer Naaman, M. O. Abutaleb, Chris Kirby, and Michael Rennie, On-chip Josephson junction microwave switch, Appl. Phys. Lett. **108**, 112601 (2016).

[19] Benjamin J. Chapman, Bradley A. Moores, Eric I. Rosenthal, Joseph Kerckhoff, and K. W. Lehnert, General purpose multiplexing device for cryogenic microwave systems, Appl. Phys. Lett. **108**, 222602 (2016).

[20] A. Baust, E. Hoffmann, M Haeberlein, M. J. Schwarz, P. Eder, J. Goetz, F. Wulschner, E. Xie, L. Zhong, F. Quijandría, *et al.*, Tunable and switchable coupling between two superconducting resonators, Phys. Rev. B **91**, 014515 (2015).

[21] Io-Chun Hoi, C. M. Wilson, Göran Johansson, Tauno Palomaki, Borja Peropadre, and Per Delsing, Demonstration of a single-photon router in the microwave regime, Phys. Rev. Lett. **107**, 073601 (2011).

[22] M. Pechal, J.-C. Besse, M. Mondal, M. Oppliger, S. Gasparinetti, and A. Wallraff, Superconducting switch for fast on-chip routing of quantum microwave fields, Phys. Rev. Appl. **6**, 024009 (2016).

[23] David M. Pozar, *Microwave Engineering* (John Wiley & Sons, USA, 2009).

[24] Samuel Goldstein, Guy Pardo, Naftali Kirsh, Niklas Gaiser, Ciprian Padurariu, Björn Kubala, Joachim Ankerhold, and Nadav Katz, Compact itinerant microwave photonics with superconducting high-kinetic inductance microstrips, New J. Phys. **24**, 023022 (2022).

[25] Friedrich Wulschner, Jan Goetz, Fabian R. Koessel, Elisabeth Hoffmann, Alexander Baust, Peter Eder, Michael Fischer, Max Haeberlein, Manuel J. Schwarz, Matthias Pernpeintner, *et al.*, Tunable coupling of transmission-line microwave resonators mediated by an rf SQUID, EPJ Quantum Technol. **3**, 1 (2016).

[26] Camille Papon, Xiaoyan Zhou, Henri Thyrrestrup, Zhe Liu, Søren Stobbe, Rüdiger Schott, Andreas D. Wieck, Arne Ludwig, Peter Lodahl, and Leonardo Midolo, Nanomechanical single-photon routing, Optica **6**, 524 (2019).

[27] Julia Zotova, Rui Wang, Alexander Semenov, Yu Zhou, Ivan Khrapach, Akiyoshi Tomonaga, Oleg Astafiev, and Jaw-Shen Tsai, Compact superconducting microwave resonators based on Al-AlO_x-Al capacitors, Phys. Rev. Appl. **19**, 044067 (2023).

[28] Martin Sandberg, C. M. Wilson, Fredrik Persson, Thilo Bauch, Göran Johansson, Vitaly Shumeiko, Tim Duty, and Per Delsing, Tuning the field in a microwave resonator faster than the photon lifetime, Appl. Phys. Lett. **92**, 203501 (2008).

[29] Zijun Chen, Anthony Megrant, Julian Kelly, Rami Barends, Joerg Bochmann, Yu Chen, Ben Chiaro, Andrew Dunsworth, Evan Jeffrey, J. Y. Mutus, *et al.*, Fabrication and characterization of aluminum airbridges for superconducting microwave circuits, Appl. Phys. Lett. **104**, 052602 (2014).

[30] Yu Zhou, Zhihui Peng, Yuta Horiuchi, O. V. Astafiev, and J. S. Tsai, Tunable microwave single-photon source based on transmon qubit with high efficiency, Phys. Rev. Appl. **13**, 034007 (2020).

[31] https://rscf.ru/en/project/21-72-30026.